Comparison of Quantum Dynamics and Quantum Transition State Theory Estimates of the H + CH$_4$ Reaction Rate[†]

Stefan Andersson,[‡] Gunnar Nyman,*[,‡] Andri Arnaldsson,[§] Uwe Manthe,[||] and Hannes Jónsson*[,§]

Department of Chemistry, Physical Chemistry, University of Gothenburg, SE-41296 Gothenburg, Sweden, Science Institute, University of Iceland, Dunhaga 3, IS-107 Reykjavík, Iceland, and Theoretische Chemie, Universität Bielefeld, Universitätsstrasse 25, D-33615 Bielefeld, Germany

Thermal rate constants are calculated for the H + CH$_4$ → CH$_3$ + H$_2$ reaction employing the potential energy surface of Espinosa-García (Espinosa-García, J. *J. Chem. Phys.* **2002,** *116,* 10664). Two theoretical approaches are used. First, we employ the multiconfigurational time-dependent Hartree method combined with flux correlation functions. In this way rate constants in the range 225−400 K are obtained and compared with previous results using the same theoretical method but the potential energy surface of Wu et al. (Wu, T.; Werner, H.-J.; Manthe, U. *Science* **2004,** *306,* 2227). It is found that the Espinosa-García surface results in larger rate constants. Second, a harmonic quantum transition state theory (HQTST) implementation of instanton theory is used to obtain rate constants in a temperature interval from 20 K up to the crossover temperature at 296 K. The HQTST estimates are larger than MCTDH ones by a factor of about three in the common temperature range. Comparison is also made with various tunneling corrections to transition state theory and quantum instanton theory.

1. Introduction

Thermal rate constants are of central importance in many chemical contexts. Accurate rate constants are usually obtained by experimental measurements, but for simple systems theoretical calculations are becoming increasingly competitive. Presently reactions of methane with different atoms provide the benchmark examples which define the state of the art for accurate, first principle based reaction dynamics studies. The H + CH$_4$ → CH$_3$ + H$_2$ reaction has been in the focus of theoretical development.[1−23] Considering in particular rigorous quantum dynamics calculations for reaction rates, calculations for the six-atom reactions H + CH$_4$ → CH$_3$ + H$_2$,[19−23] its isotopically substituted variants D + CH$_4$[23] and CH$_3$ + H$_2$/HD/D$_2$,[24] and the O + CH$_4$ → CH$_3$ + OH reaction[26] represent the present limit. The computational method used in these studies combines the multiconfigurational time-dependent Hartree approach (MCTDH)[27,28] with flux correlation functions.[29−31] These quantum dynamics studies are quite demanding, and it is of interest to develop less computationally demanding and still reliable methods for rate constant calculations. To be able to treat tunneling in larger molecular systems, transition state theory (TST) based approaches seem to be ideal. Following this idea, the present work will investigate the recently developed harmonic quantum transition state theory (HQTST)[32] implementation of instanton theory, apply it to the H + CH$_4$ reaction, and compare the results with accurate quantum dynamics results and results from other TST-based approaches.

In transition state theory a dividing surface is defined which minimizes the flux between reactants and products. Conventional harmonic transition state theory approximates the dividing surface as a hyperplane that contains the saddle point on the minimum energy path that connects the reactants and products. TST completely neglects the effects of tunneling and recrossing of the transition state. In a proper quantum treatment of a chemical reaction it is not possible to separate tunneling from recrossing as they are intrinsically interwoven. HQTST approximately accounts for these effects by lowering the effective barrier height for the reaction. We assess here how well this works for the H + CH$_4$ → CH$_3$ + H$_2$ reaction.

Within the context of transition state theory, quantum delocalization effects can be added in all bound degrees of freedom by using quantum partition functions. This is most commonly done by using the harmonic approximation and calculating the vibrational partition functions for a collection of 1D quantum harmonic oscillators. However, motion through a barrier cannot be treated in such a straightforward way. There are two main approaches to dealing with quantum tunneling in TST. The most common approach is to calculate a tunneling correction factor to conventional (variational) TST. This is done by defining tunneling paths and calculating the semiclassical imaginary action along these paths. This was first suggested by Marcus[33] and has since then been developed into a successful suite of methods by Truhlar and co-workers[34−39] implemented into the POLYRATE program.[40] Alternatively, different versions of quantum transition state theory (QTST) have been developed. Various approaches for approximations have been tried, and those based on the imaginary time Feynman path integral[41,42] (FPI) have been particularly successful,[43−49] which is also the basis of HQTST. These methods require the specification of some dividing surface separating reactants and products just as in conventional TST. However, the Heisenberg uncertainty principle makes it impossible to have a well-defined dividing surface in configuration space since both the positions and momenta of the particles have to be exactly defined at the same point. This has made it necessary to extend the definition and

---

Comparison of H + CH₄ Reaction Rates

J. Phys. Chem. A, Vol. 113, No. 16, 2009 **4469**

develop new methods to identify a dividing surface for quantum mechanical systems.

One particularly simple version of FPI based rate theory is the instanton theory. Instanton theory was developed independently by researchers in chemical physics[50] and quantum field theory[51,52] in the 1970s. It has found widespread use in quantum field theory[53,54] but has so far only found limited use in the chemical physics community. The theory is formally equivalent to the ImF[55−57] (imaginary free energy) theory of the rate of escape from metastable states. Miller and co-workers[58] applied instanton theory to the collinear H + H₂ reaction and found good agreement with accurate quantum dynamics results. Benderskii and co-workers[59] recognized the potential of instanton theory for low-temperature chemical systems and applied it to two-dimensional test problems. Due to problems of implementing an efficient routine to calculate periodic orbits, "instantons", on the upside-down potential, which is the traditional approach, the method was not used for studies of systems with more degrees of freedom. Siebrand and co-workers[60,61] have developed the approximate instanton method, in which one-dimensional (1D) motion along the reaction path is separated from the rest of the system. It is then more or less trivial to find the instanton along this reaction path. To calculate rate constants the instanton action is needed and this is done by correcting the basic 1D instanton action by terms from the modes that are orthogonal to the reaction path. This method has been successfully applied to calculating unimolecular rate constants and tunneling splittings in relatively large molecular systems in an efficient manner.

The recently developed harmonic quantum transition state theory (HQTST)[32] is an implementation of instanton theory which is based on the fact that the instantons are stationary points of the Euclidean action or more precisely (first-order) saddle points.[62] By basing the implementation on imaginary time FPIs, it has been possible to recast the search for an instanton as an efficient saddle-point search on a generalized temperature-dependent potential energy surface or an "action surface". This has made it possible to apply instanton theory to multidimensional systems without invoking any approximations other than purely numerical ones. HQTST generally requires much fewer force calls than methods where a full (Monte Carlo) evaluation of properties using FPIs is required. The HQTST method can therefore be combined with first principles evaluations of the forces. While this aspect is not used in the present work, it suggests that HQTST may become highly useful in many contexts of rate constant calculations. HQTST has previously been found to perform well, but somewhat underestimate the rate constants at low temperature, for one- and two-dimensional model problems where accurate results are available.[32] It is thus of great interest to evaluate HQTST also for real chemical reactions that involve more degrees of freedom.

The TST-based theories discussed above all require different approximations, and it is necessary to validate the accuracy of the approximate approaches by comparing with exact quantum dynamics results. Tests for the H + CH₄ reaction rate have already been provided for the tunneling corrected TST approach of Truhlar and co-workers.[12] These tests employed the Jordan−Gilbert potential energy surface,[63] which was used for the first accurate quantum dynamics calculation studying the H + CH₄ reaction.[19−21] More recent work applying the quantum instanton approach of Miller et al.[49] to the H + CH₄ reaction,[64] however, employed the newer potential energy surface of Espinosa-García[16] (PJEG). The main goal of the present work is to apply the HQTST approach to the H + CH₄ reaction and

to compare the results with accurate quantum dynamics results and the results of the other TST-based theories. Since quantum instanton results are available only for the PJEG PES, this PES will be employed in the present work. However, accurate quantum dynamics results for this PES have not been published up to now. Therefore in the present work such calculations using the MCTDH-flux correlation function approach will be performed. These results then also allow for a comparison of rate constants for the PJEG PES with the rate constant obtained for the more accurate WWM PES.[22,23]

The paper is organized as follows. Section 2 discusses the two theoretical approaches employed in this work. The section is divided into two parts, where part 1 briefly describes the MCTDH reaction rate calculations and part 2 briefly describes the HQTST calculations. Section 3 gives numerical details, and in section 4 results are presented and discussed. We conclude with a summary and some final remarks.

2. Theory

2.1. Quantum Dynamics Calculations of Reaction Rate Constants. The present work uses the approach introduced in ref 65 to accurately calculate reaction rates by quantum dynamics simulations. The approach combines MCTDH wave packet propagation[27,28] with the use of flux-correlation functions[29−31] and an efficient evaluation of ensemble averages.[66,67] As a result, the cumulative reaction probability for vanishing total angular momentum is obtained for the given PES.

Assuming that the J-shifting[68] approximation is valid, then the rate constant $k(T)$ at a temperature T is calculated from

$$k(T) = \frac{Q_{\text{rot}}^{\ddagger}(T)}{2\pi\hbar Q_{\text{r}}(T)} \int \text{d}E \, N(E) \exp(-E/k_{\text{B}}T) \qquad (1)$$

where $Q_{\text{rot}}^{\ddagger}(T)$ is the rotational partition function for the transition state, $Q_{\text{r}}(T)$ is the reactant partition function, E is the total energy, and $N(E)$ is the cumulative reaction probability for total angular momentum $J = 0$. The reactant partition function can be determined by accurate quantum dynamics calculations employing MCTDH propagation in imaginary time.[69] However, typically sufficiently accurate $Q_{\text{r}}(T)$ values can be obtained by calculating only the zero point energy exactly, employing the harmonic approximation to describe vibrational excitations, and using a classical approximation for rotational and translational motions.[69,70] This simplified scheme yields a sufficiently accurate partition function of CH₄ in the temperature range investigated in the present work,[69] and it is therefore employed here.

The cumulative reaction probability obtained from the quantum simulations can be written as a sum of several terms $N_i(E)$: $N(E) = \sum_i N_i(E)$, [71] where each $N_i(E)$ corresponds to a pair of eigenstates of the thermal flux operator. The contribution $N_i(E)$ to $N(E)$ can be viewed as the contribution of the ith vibrational state of the activated complex. It is thus possible to use $N_0(E)$ to calculate a contribution $k_0(T)$ to $k(T)$ from the ground vibrational state of the activated complex.

$$k_0(T) = \frac{Q_{\text{rot}}^{\ddagger}}{2\pi\hbar Q_{\text{r}}} \int \text{d}E \, N_0(E) \exp(-E/k_{\text{B}}T) \qquad (2)$$

Using a harmonic approximation for the vibrational partition function of the transition state referenced to the ground vibrational state of the activated complex, $Q_{\text{ho}}^{\ddagger}$, we can write

4470 *J. Phys. Chem. A, Vol. 113, No. 16, 2009*

Andersson et al.

$$k_{\text{ho}}(T) = \frac{Q_{\text{rot}}{}^{\ddagger}Q_{\text{ho}}{}^{\ddagger}}{2\pi\hbar Q_{\text{r}}} \int dE\, N_0(E) \exp(-E/k_{\text{B}}T) \quad (3)$$

If the $N_i(E)$ values obey

$$N_i(E) = N_0(E - (E_i - E_0)) \quad (4)$$

then eq 3 is identical to eq 1. The expression in eq 4 can therefore be considered as a vibrational analogue to the *J*-shifting approximation[68] for rotational motion, meaning that the vibrational motions orthogonal to the reaction path are dealt with as the overall rotation of the complex in the *J*-shifting approximation.

The approximate expression for the rate constant, eq 3, can easily be related to harmonic transition state theory (HTST). HTST assumes that $N_0(E) = \Theta(E - E_{\text{b}})$, where Θ is the Heaviside step function and E_{b} is the vibrationally adiabatic ground-state barrier height in the harmonic approximation. Using this we have that $\int dE\, N_0(E) \exp(-E/k_{\text{B}}T) = k_{\text{B}}T \exp(-E_{\text{b}}/k_{\text{B}}T)$ and obtain

$$k^{\text{HTST}}(T) = k_{\text{B}}T \frac{Q_{\text{rot}}{}^{\ddagger}Q_{\text{ho}}{}^{\ddagger}}{2\pi\hbar Q_{\text{r}}} \exp(-E_{\text{b}}/k_{\text{B}}T) \quad (5)$$

Finally, it should be noted that if the harmonic approximation is used for the transition state, it should also be used for the reactant partition function.[70] However, if the energy of the vibrational ground state of the activated complex includes anharmonic effects, as in eq 3, then this should also be the case for the reactant partition function.

2.2. Harmonic Quantum Transition State Theory Calculation of Reaction Rate Constants. The harmonic quantum transition state theory (HQTST) implementation employed here builds on the instanton implementation of Arnaldsson and Jónsson.[32] They have applied HQTST to one- and two-dimensional model problems and to reactions occurring on solid surfaces and in the gas phase.[32] For low-dimensional systems, analytic potentials were used, but tunneling in multidimensional systems was studied using forces calculated directly by density functional theory (DFT). This shows that HQTST is also of practical use in a "direct dynamics" implementation, where rate calculations are interfaced with an electronic-structure code. Here we give a brief summary of the HQTST method with emphasis on the features of relevance to the present study.

Quantum mechanical partition functions may be evaluated as the trace of the density matrix. That is, only the diagonal of the density matrix is needed, and using Feynman path integrals this means that only closed paths have to be included. These closed Feynman paths (CFPs) have a period of $\hbar/(k_{\text{B}}T)$. In HTST the rate constant is obtained by evaluating partition functions at the point of highest energy along the minimum energy path (MEP), which is a saddle point, leading from reactants to products. This choice is made as the MEP is the path of highest statistical weight in classical systems. The quantum mechanical analogue of the MEP is the minimum action path (MAP).[46,72] It connects reactants and products such that the Euclidean action along the path is minimized. This is the path that contributes most to the quantum partition function. Along the MAP, each point is a CFP. The CFP of maximum action along the MAP is a saddle point of the action and is called the instanton.

The Euclidean action of the CFP can be written[42]

$$S_{\text{E}} = \int_0^{\hbar/k_{\text{B}}T} H\, d\tau \quad (6)$$

where H is the classical Hamiltonian of the system and τ is the magnitude of imaginary time. In its discretized form the CFP can be represented by a cyclic chain of images of the system,[73] or "system replicas" or "beads", connected by temperature-dependent harmonic spring forces. Using this representation the Euclidean action is calculated as[46]

$$S_{\text{E}}(q) = \frac{\hbar}{k_{\text{B}}T} \sum_{k=1}^{P} \left[\frac{k_{\text{sp}}(T)}{2} \left| q_{\text{mod}(k,P)+1} - q_k \right|^2 + \frac{V(q_k)}{P} \right] = \frac{\hbar V_{\text{eff}}(q, T)}{k_{\text{B}}T} \quad (7)$$

where the spring constants are given as

$$k_{\text{sp}}(T) = \mu P \left(\frac{k_{\text{B}}T}{\hbar} \right)^2 \quad (8)$$

P is the number of images, q_k are coordinates of image k, $V_{\text{eff}}(q, T)$ is an effective potential energy surface, and μ is the mass of the degree of freedom in question. Subscript mod results from the path being closed so that image P is connected to image 1. The rightmost part of eq 7 makes it clear that weighting each closed path in the quantum partition function by $\exp(-S_{\text{E}}(q)/\hbar)$ is equivalent to weighting by $\exp(-V_{\text{eff}}(q, T)/(k_{\text{B}}T))$.

Above the crossover temperature[43,59,62]

$$T_{\text{c}} = \frac{\hbar\omega^{\ddagger}}{2\pi k_{\text{B}}} \quad (9)$$

all images collapse onto a single point, the classical saddle point along the MEP. Here $\omega^{\ddagger}$ is the magnitude of the imaginary frequency at the classical saddle point. This collapse results from the spring constant k_{sp} becoming larger than the curvature of the real potential. Below T_{c} tunneling is the dominant transition mechanism.

As mentioned above, the instanton is a saddle point of the Euclidean action. Using a discretized CFP, the corresponding "action surface", given by $S_{\text{E}}(q)$, has NP dimensions where N is the number of degrees of freedom of the physical system and P is the number of images in the CFP. To find the instanton therefore requires a saddle-point optimization in an NP-dimensional space.

In HTST the rate constant is found by expanding the potential energy surface to second order at the saddle point. An analogous procedure in the quantum case is to expand the action, or equivalently V_{eff}, to second order at the instanton, which results in an instanton rate constant[45]

$$k_{\text{inst}} = \frac{1}{Q_{\text{r}}} \sqrt{\frac{S_0}{2\pi\hbar}} \frac{1}{\Delta\tau \left| \prod_j' \lambda_j \right|} \exp[-V_{\text{eff}}(q_{\text{inst}}, T)/(k_{\text{B}}T)] \quad (10)$$

Here index inst stands for instanton, $\Delta\tau = \tau/P = \hbar/(k_{\text{B}}TP)$ is the imaginary time step, and λ_j are generalized vibrational frequencies of the instanton chain. For a system of N degrees of freedom there are $NP - 2$ real nonzero frequencies, one

Comparison of H + CH₄ Reaction Rates

J. Phys. Chem. A, Vol. 113, No. 16, 2009 **4471**

imaginary frequency corresponding to the unstable instanton mode, and one zero-valued frequency corresponding to the "zero mode" resulting from a rotation of the chain of images, i.e., shifting the images along the instanton. The prime on the product of frequencies in eq 10 indicates that the zero frequency is not included in the product. Instead, with the zero mode there is associated an action

$$S_0 = \frac{\mu k_B TP}{\hbar} \sum_k^P (q_{\text{mod}(k,P)+1} - q_k)^2 \tag{11}$$

which is twice the free-particle instanton action.

Expanding to second order is equivalent to using the harmonic approximation for the contributions to the partion function from each system replica of the instanton. The expansions are not done at the saddle point on the classical potential but at the geometries of the system replicas. These geometries reflect the full potential energy surface, not just a harmonic approximation around the classical saddle point. The assumption in instanton theory is that the instanton is the dominant tunneling path and only paths in its vicinity will contribute significantly to tunneling. Instead of evaluating the action of these additional paths explicitly, a harmonic expansion is made along the instanton to calculate the rate constant in an efficient, albeit approximate, manner. As described in section 2.1, in the quantum dynamics we always find the ground-state flux anharmonically at the transition state but have the option of harmonically approximating the excited states.

The discussion so far is relevant to reactions that occur on or inside a solid where only vibrational motion has to be considered. For gas-phase reactions also translational and rotational motions must be considered. In HQTST it is assumed that translational, rotational, vibrational, electronic, and nuclear degrees of freedom are separable. Note that for the present study of the H + CH₄ reaction this was also done in the quantum dynamics evaluation of the rate constant. Electronic and nuclear degrees of freedom can be left out for the present application. Thus we add contributions from translational and rotational motions to k_{inst}. For the present application these can be treated classically.

We have until now only discussed the partition functions at the transition state. The reactant partition function however also has to be evaluated. The translational and rotational contributions are evaluated classically. To be consistent with the harmonic evaluation of the vibrational modes of the instanton, also the vibrational reactant partition function is evaluated harmonically in HQTST.

3. Numerical Details

In this section we discuss some of the numerical details pertaining to the MCTDH and the HQTST calculations.

3.1. Quantum Dynamics. The present work uses the computational approach introduced in ref 65. The approach has already previously been applied to the H + CH₄→ CH₃ + H₂ reaction[19,20,22,23] using other PESs. Therefore the details of the approach will not be repeated here and only specific details relevant to the present application will be given. The coordinates used in the propagation are obtained by first finding the normal mode coordinates of the transition state and then, for numerical reasons, making a linear transformation of two of the modes.[19,20] Here the transformation is such that mode 1, the mode with the imaginary frequency, is mixed with mode 9

$$\begin{pmatrix} Q_1' \\ Q_9' \end{pmatrix} = \begin{pmatrix} \cos\gamma & -\sin\gamma \\ \sin\gamma & \cos\gamma \end{pmatrix} \begin{pmatrix} Q_1 \\ Q_9 \end{pmatrix} \tag{12}$$

The two modes Q_1 and Q_9 largely correspond to motions of the H atoms located on the C_{3v} symmetry axis. Here we set $\gamma = -135°$. The dividing surface can now be defined as $Q_1' = 0$, and the transformed coordinates Q_i' are employed in the wavepacket propagation.

The parameters used to represent the wave function, the numbers of single particle functions and the grid sizes, have been determined by convergence tests. The procedure is lengthy but has been described in refs 20, 21, and 23. Table 1 gives the parameters used in the converged calculations.

An important parameter in the quantum dynamics simulations is the reference temperature T_{ref}.[74,75] While the results are formally independent of T_{ref}, they are numerically dependent on it as T_{ref} determines the energy range in which $N(E)$ can be reliably computed. In the present study T_{ref} was set to 300 K.

3.2. HQTST. The HQTST calculations are performed in Cartesian coordinates, i.e., no special internal coordinates have to be specified and the number of degrees of freedom, N, is 18 instead of 12 as in the MCTDH calculations. First, a choice is made of the number of images, P, in the discretized CFP used to optimize the instanton. In our calculations P has been varied between 16 and 1024 to test convergence.

In order to initialize the calculations, first the classical saddle point is optimized. This will facilitate the calculations since the instanton coincides with the classical saddle point at the crossover temperature T_c (eq 9). For the PJEG surface the imaginary frequency at the saddle point is $1293i$ cm⁻¹, which gives $T_c = 296.2$ K. Therefore, the first instanton optimization has been performed at a temperature just below T_c, in this case at 295 K. As an initial guess for the CFP chain, the images are distributed within a small distance from the classical saddle point along the corresponding unstable normal mode. Then the instanton has been found and optimized using a saddle-point finding algorithm of the minimum-mode following type[76] with a Lanczos iterative approach to finding the minimum mode.[77] Note that this saddle-point optimization is performed on the NP-dimensional action surface as discussed in section 2.2. For the case of 1024 images this therefore requires optimization in 18432 dimensions.

Note that above T_c the instanton collapses onto the classical saddle point. Even though the instanton can be (trivially) optimized above T_c the algorithm will not give any sensible rate constants so it makes no sense to apply HQTST at higher temperatures.

It has been found that the instanton chain does not form open ring structures.[32] Rather the images in the chain collapse pairwise onto a "stringlike" structure. Therefore the calculations only require forces to be calculated for half of the images since they will be pairwise equivalent to the other half. Such a collapsed structure is enforced in our calculations since it has clear advantages with respect to computational effort.

Once the instanton is optimized to within a sufficient force convergence criterion the optimization is stopped. Generally, a maximum force of $10^{-4} - 10^{-3}$ eV Å⁻¹ will ensure sufficiently converged rate constants, but in this case the convergence criterion was set to 10^{-6} eV Å⁻¹ to make sure that there is no significant numerical uncertainty in the calculated rate constants. Following optimization the calculation of the normal-mode frequencies of the instonton is performed. These are the frequencies that enter into the calculation of the rate constant,

TABLE 1: Parameters for the MCTDH Representation of the Wavefunction

coordinate	no. of single-particle functions	grid size	grid type	grid range for FFT (a.u.)
Q_1'	7	48	FFT	$[-100, 140]$
Q_2/Q_3	4	15	Hermite DVR	
Q_4	3	32	FFT	$[-100, 100]$
Q_5/Q_6	3	10	Hermite DVR	
Q_7/Q_8	2	8	Hermite DVR	
Q_9'	5	48	FFT	$[-155, 85]$
Q_{10}	2	8	Hermite DVR	
Q_{11}/Q_{12}	3	8	Hermite DVR	

k_{inst} (eq 10). As mentioned in section 2.2 there should be $NP - 2$ real nonzero frequencies, one imaginary and one zero-valued frequency.

When the first instanton has been optimized, it can subsequently be used as initial guess for an instanton optimization at a somewhat lower temperature. The same procedure can then be followed for calculations at yet lower temperatures. As the harmonic spring constants connecting the images (eq 8) become smaller with decreasing temperature, the instanton will spread out more and more. Note that the instanton is in no way constrained to remain connected to the classical saddle point, the minimum energy path, or any other point in configuration space. Its shape will be solely decided by the location of the instanton saddle point in action space.

The spacing of consecutive temperatures is typically around 10 K. However, at low temperatures it might be necessary to make this spacing smaller. In principle it seems as the most efficient manner to proceed is to have *inverse* temperatures that are roughly equally spaced rather than to have equal spacing in temperature. Given a reasonable initial guess the optimization of the instanton will require on the order of 10^2 force calls per image for the smallest numbers of images considered and up to 10^3-10^4 force calls per image for the largest numbers of images. At least part of the increase of the number of force calls can be related to the decreasing forces from the PES on each image as the number of images is increased (see eq 7). The optimization for a large number of images can therefore be perturbed by numerical noise, which leads to slower convergence.

Below a given temperature a second imaginary frequency can appear among the instanton frequencies. This is a clear sign that the number of images is insufficient and needs to be increased. The calculation of the rate constant might still give a reasonable result, but already above this temperature the rate constants will have started to deviate significantly from the fully converged results (see section 4.2).

The reactant vibrational partition function that enters in the calculation of the instanton rate constant (eq 10) is not calculated using the analytic expression for the quantum harmonic oscillator as done in standard TST. To be consistent with the evaluation of the instanton vibrations, it is calculated as the vibrational partition function of a CFP located at the reactant minimum. This CFP has the same number of images as the one used to describe the instanton. With all images collapsed to one point the normal mode calculation will therefore include a combination of force constant terms from the minimum of the potential energy surface and the spring constants of the CFP.[32]

To calculate the rotational partition function of the instanton, it is treated as a classical rotor. The moments of inertia of each image in the instanton chain are evaluated, and finally the geometric mean of these moments of inertia is calculated and used in the instanton rotational partition function. An alternative would be to treat the whole instanton as a "supermolecule" and

calculate its moments of inertia.[32] In fact the two approaches produce almost equal results and give differences in the calculated HQTST rate constants of at most 6% (at 20 K). Note that for the MCTDH rate constant calculations the classical saddle point geometry is used to evaluate the transition state rotational partition function. However, the difference between the instanton and saddle point rotational partition functions is at most 8% in the range of temperatures where the HQTST and MCTDH calculations are compared.

4. Results and Discussion

We begin this section by comparing our rate constants obtained from the present quantum dynamics calculations employing PJEG to previous rate constant calculations using the same methodology but the Shepard interpolated potential energy surface[23] (section 4.1). Thereafter, in section 4.2, we compare the presently obtained quantum dynamics and HQTST rate constants on PJEG to each other and illustrate the HQTST calculations. We also compare the rate constants to previously obtained quantum instanton[64] and transition state theory rates on PJEG. In section 4.3 the convergence of the HQTST calculations is evaluated, and in section 4.4 the conceptual and visual benefits of studying tunneling using HQTST are discussed.

**4.1. Quantum Dynamics Rates on Different Potentials.** The present work focuses on the PJEG potential energy surface of Espinosa-García.[16] Reaction rates for this PES have been published using several different approximate quantum transition state approaches. Therefore this PES provides an ideal example for a comparison of quantum transition state theories.

However, the PJEG PES is a semiempirical potential energy surface based on a functional form similar to the older and widely used Jordan and Gilbert PES.[63] Rate constants calculated using a tunneling corrected version of transition state theory, CVT/μOMT,[34−39] have been used to calibrate parameters employed in the definition of the PJEG PES. Recently, more accurate ab initio based potential energy surfaces for the H + $CH_4 \rightarrow CH_3 + H_2$ reaction have become available. The WWM PES[22,23] employs high level ab initio data and a Shepard interpolation approach to provide a very accurate description in the vicinity of the reaction barrier and to thereby facilitate the calculation of reaction rates with a controlled accuracy.

In Figure 1, accurately calculated thermal rate constants for the PJEG surface obtained in the present work by the MCTDH approach are shown. The rate constants computed for the PJEG surface are compared with the accurate rate constants previously calculated using the WWM surface. It is seen that the PJEG surface results in rate constants that are approximately a factor 3 to 4 larger than the WWM rates. It is not surprising that the PJEG rate constants are larger as the barrier height is substantially lower (12.9 vs 14.93 kcal/mol). Actually, the fact that the difference is not larger reflects that there are also other differences. The imaginary frequency at the saddle point, for example, is lower on the PJEG surface ($1293i$ vs $1414i$ cm^{-1}).
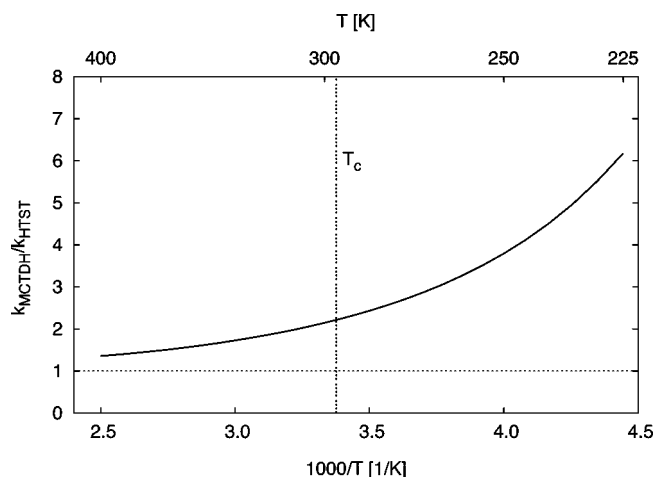
Comparison of H + CH₄ Reaction Rates

J. Phys. Chem. A, Vol. 113, No. 16, 2009 **4473**
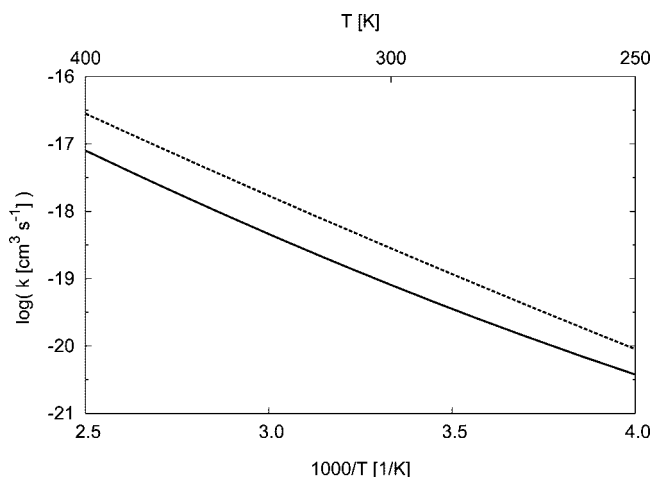
Figure 1. Accurate quantum dynamics rate constants for $H + CH_4 \rightarrow H_2 + CH_3$ using the Shepard interpolated potential (solid line) (ref 22) and PJEG (dashed line).
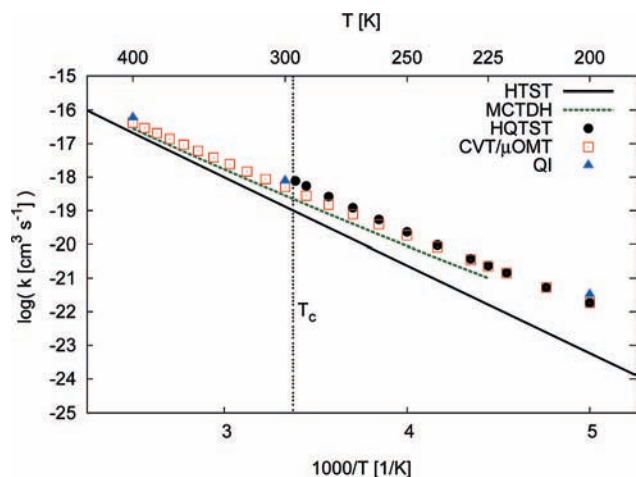
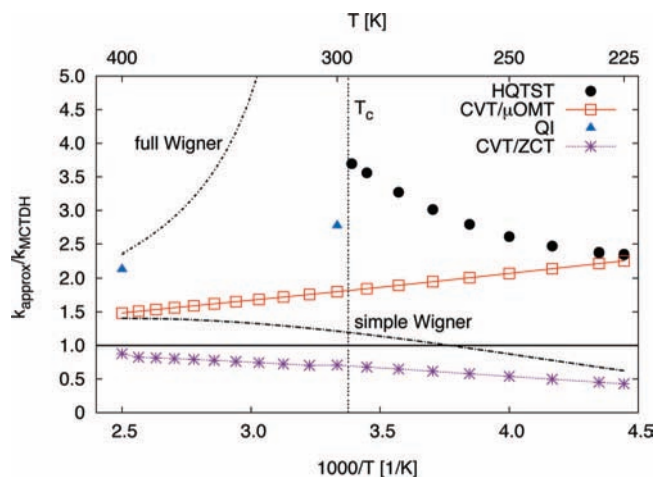**Figure 2.** Rate constants for the $H + CH_4 \rightarrow CH_3 + H_2$ reaction using PJEG. The accurate quantum dynamics rate constants are denoted MCTDH. QI refers to quantum instanton rate constants.[64] T_c denotes the crossover temperature. See the text for details.

Figure 3. The ratio of MCTDH rate constants and HTST rate constants as function of temperature.

Figure 4. The ratio of the rate constants of approximate rate theories and MCTDH accurate rate constants. See the text for details.

4.2. Accurate and Approximate Rate Constants. We begin this section by comparing the rate constants calculated on PJEG using accurate quantum dynamics to the HQTST rate constants obtained on the same surface. In Figure 2 these rate constants are shown. It can be seen that HQTST gives rate constants that are about a factor of 3 larger than the quantum dynamics based rate constants. Figure 2 also shows results from harmonic transition state theory (HTST). In HTST the vibrational partition functions are evaluated quantum mechanically in the harmonic approximation and rotations are treated as classical rigid rotors. No account is taken of tunneling, and therefore these rate constants become smaller than the others as the temperature is lowered. Also included in the figure is a tunneling corrected TST, the canonical variational theory with microcanonically optimized multidimensional tunneling (CVT/μOMT), where the calculations have been performed with the POLYRATE code[40] in the same way as in the paper by Espinosa-García,[16] which included results for only a limited number of temperatures. CVT/μOMT seems to somewhat overestimate the effect of tunneling but is still in better agreement with MCTDH than HQTST down to 225 K, where the two approximate methods give approximately equal results. The quantum instanton (QI) method[49] was derived to create an instanton-like theory using the quantum Boltzmann operator in the derivation of the theory rather than

the approximate semiclassical Boltzmann operator as in standard instanton theory. In QI there is no instanton path and the rates are evaluated using Path Integral Monte Carlo methods. We will return to the QI results[64] shown in Figure 2.

Figure 3 shows the ratios of the MCTDH rate constants and the HTST rate constants on the PJEG surface. It is seen that this ratio increases with decreasing temperature as expected. At $T_c = 296$ K MCTDH gives a rate constant that is more than a factor 2 larger than HTST, so below T_c tunneling will dominate the rate constant. At the lowest temperature considered, 225 K, the MCTDH rate constant is 6 times larger than the HTST rate constant. It should be noted that the increase of the rate constant due to tunneling is significantly smaller for the PJEG PES than for the more accurate WWM PES.

In Figure 4 the ratios of rate constants obtained from the approximate methods and the MCTDH rate constants are shown for the $H + CH_4 \rightarrow CH_3 + H_2$ reaction on PJEG in the temperature range 225–400 K. Apart from the approximate methods already shown in Figure 2 this also includes three common versions of tunneling corrections applied to transition state theory. One of these uses an analytic exact tunneling correction for a parabolic barrier

$$\kappa(T) = \frac{\hbar\omega^{\ddagger}/2k_BT}{\sin(\hbar\omega^{\ddagger}/2k_BT)} \quad (13)$$

which was first derived by Wigner.[78] This will be referred to as "full Wigner". The rates obtained in this way become singular as the temperature is lowered to reach the crossover temperature. Therefore we do not show it for temperatures below T_c. Another is the popular "simple" Wigner correction[59,79,80]

$$\kappa(T) = 1 + \frac{1}{24}(\hbar\omega^{\ddagger}/k_B T)^2 \qquad (14)$$

which is an expansion of eq 13 to third order. Such an approximation is expected to work reasonably well if the tunneling contribution to the rate constant comes from tunneling close to the top of the barrier, i.e., if tunneling is of small to moderate importance compared to classical "over-the-barrier" transitions. This is what should be the case above T_c but not below. In the temperature range shown, the simple Wigner correction accounts for tunneling resonably well.

Also shown in Figure 4 are results from CVT/ZCT, which we obtain using the POLYRATE program.[40] ZCT stands for zero curvature tunneling and is a less sophisticated tunneling correction than that used in CVT/μOMT, which picks the larger of two tunneling corrections (SCT = small curvature tunneling and LCT = large curvature tunneling). In ZCT the tunneling path is assumed to lie along the minimum energy path, while in SCT and LCT "corner-cutting" is included. Tunneling paths will generally be shorter than the path along the MEP, i.e., they "cut the corner" of the potential energy surface. However, also CVT/ZCT produces rate constants in good agreement with the accurate ones in the temperature range shown. In the case of H + CH$_4$ corner-cutting therefore does not seem to be so pronounced in this temperature range (see section 4.4). It should also be noted that the CVT/μOMT rate constants are practically identical to the CVT/SCT results indicating that the tunneling paths are relatively close to the MEP. CVT/μOMT and HQTST show different behavior. While the ratio between the CVT/μOMT and MCTDH rate constants becomes increasingly larger as T decreases, the HQTST rate constants show the opposite behavior by a decreasing ratio with lower T.

For several one- and two-dimensional model systems Arnaldsson[32] found excellent agreement between rates obtained with HQTST and accurate quantum dynamics. The HQTST rates were typically found to be somewhat higher than the accurate ones just below T_c and slightly lower at low temperatures. Why this behavior is not seen for the case of the H + CH$_4$ reaction is not clear. Apart from the obvious fact that HQTST is a semiclassical method that does not include purely dynamic quantum effects, it is interesting to also consider the treatment of the reactant. As discussed above, the reactant partition function in the HQTST calculations has been obtained in the harmonic approximation, while "anharmonicity" to some extent is included in the instanton. Even though the instanton is a saddle-point in *action space* and a harmonic expansion is made around it to calculate the rate constant, it cannot be described as being harmonic along a reaction path in *configuration space*. The word "harmonic" would normally imply the use of a parabolic approximation to the barrier. In HQTST there is no approximation to the potential and the instanton is found by sampling the potential energy surface. When the reactant state partition function is evaluated, the CFP is collapsed at the reactant minimum, because the minimum of the potential energy surface is also a minimum in action space. Therefore it is conceptually clear that the reactant vibrational partition function should be calculated by a harmonic expansion of the CFP at the minimum, in the same way as for the instanton CFP. Because
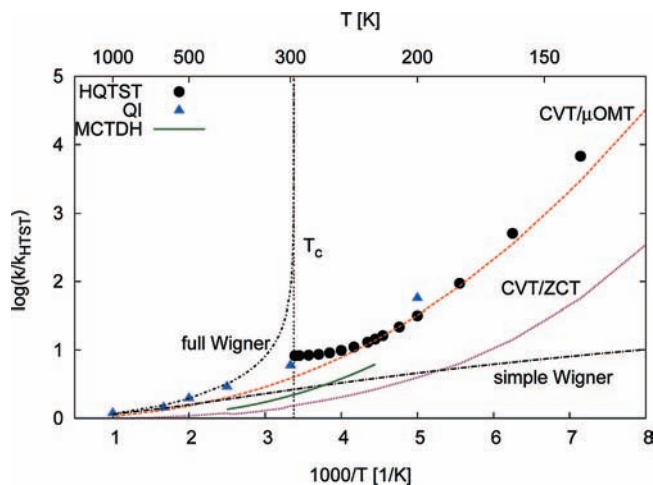
Figure 5. The ratio of rate constants for methods including tunneling and HTST rate constants.

the instanton explores some anharmonicity of the PES, one would be tempted to use an anharmonic evaluation of the reactant vibrations. Even though this is not rigorously justifiable, it could suggest to which extent the harmonic treatment of the reactant adds to the discrepancy between HQTST and accurate quantum dynamics. A limiting case would be to evaluate the reactant partition function fully anharmonically. The main effect however comes from adjusting the reactant zero point level for anharmonicity. This can be done by multiplying the rate constant by $\exp(-\Delta E_{ZPE}/RT)$, where ΔE_{ZPE} is the difference between the harmonic and the accurate zero point energy, which comes out to be 183.7 cm^{-1}. Such a correction lowers the HQTST rate constants by a factor 2.4 at 296 K and 3.2 at 225 K, which makes the agreement with the accurate rate constant much better. At the same time the typical behavior of the HQTST rate constant discussed above is recovered (cf. Figure 4). This could imply that a large part of the discrepancy between the HQTST and MCTDH rate constants comes from the harmonic approximation of the reactant. Whether this is generally true requires more investigation.

To extend the comparison between the different methods, Figure 5 shows the ratio of the different calculated rate constants and the HTST rate constants in the temperature range 125−1000 K. At temperatures well above T_c all approximate methods, except CVT/ZCT, agree quite well. As discussed above all methods agree fairly well around T_c, except the full Wigner correction, which turns singular. Down to 200 K the more elaborate approximate methods, QI, HQTST, and CVT/μOMT, agree quite well with each other and show similar temperature dependence as the MCTDH rate constants. As discussed above, a major source for this difference could be the harmonic treatment of the reactant vibrations in HQTST (and CVT/μOMT). In QI no harmonic approximations are made so it would be expected to show better agreement with MCTDH (see discussion below). At 200 K the HQTST and CVT/μOMT rate constants practically coincide, differing by only 1%, while the QI rate constant is a factor 1.8 larger than the other two. Below 200 K the HQTST and CVT/μOMT rate constants start to deviate more and more with decreasing temperature. The simple Wigner correction, which works quite well above T_c, does not give a qualitatively correct description of tunneling below T_c, as would be expected. The CVT/ZCT rate constants show a qualitatively correct behavior but fall below the more accurate

Comparison of H + CH$_4$ Reaction Rates

J. Phys. Chem. A, Vol. 113, No. 16, 2009 **4475**
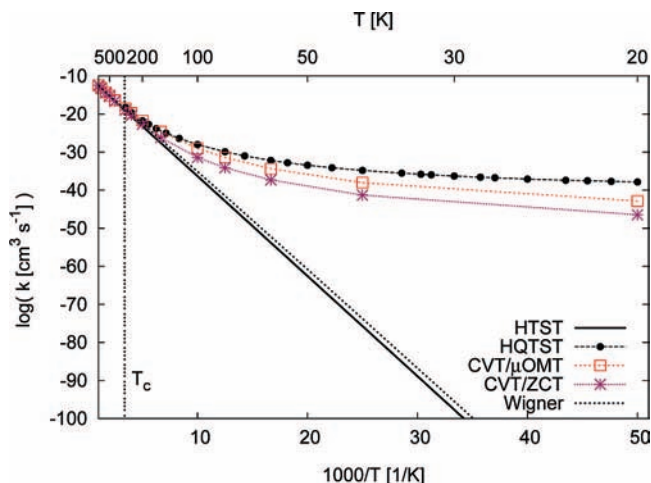
Figure 6. Rate constants for H + CH$_4$ → CH$_3$ + H$_2$ using PJEG. The keys are explained in the text.

Figure 7. MCTDH flux−flux correlation function, $C(t)$, for H + CH$_4$ using PJEG.

treatments by increasing amounts as temperature decreases. At 125 K the difference to CVT/μOMT and HQTST is 2 orders of magnitude.

The deviation between the HQTST and CVT/μOMT rate constants becomes larger as temperature is decreased further as seen in Figure 6. Here we show rate constants calculated on PJEG using HTST, HTST with the simple Wigner correction, HQTST, CVT/μOMT, and CVT/ZCT down to 20 K. This figure illustrates the need to treat tunneling accurately at low temperature. As noted above the Wigner correction cannot treat tunneling even qualitatively correct below T_c so it is just included for comparison. The HQTST, CVT/μOMT, and CVT/ZCT rate constants seem to account for tunneling in a qualitatively correct way. At 20 K the HQTST rate constant is 5 orders of magnitude larger than the CVT/μOMT rate constant and 9 orders of magnitude larger than the CVT/ZCT rate constant. However, the HQTST rate constant is 104 orders of magnitude larger than the HTST rate constant at 20 K. At the lowest temperatures the rate constants are likely too small to be measurable in experiments. The main reason for including them is to demonstrate that HQTST is able to treat tunneling at temperatures that are considerably lower than T_c. Accurate quantum dynamics results are not included as we are not able to conclusively converge those calculations below 225 K. Therefore it is difficult to estimate the quality of the calculated rate constants. However, it has previously been shown that HQTST gives better agreement with quantum dynamics than TST with a small-curvature tunneling correction for model systems at low temperatures.[32] There it was also noted that the HQTST and SCT results agreed well close to T_c, as also seen for H + CH$_4$ (see Figures 2, 4, and 5). If this is generally true, an efficient way of calculating rate constants including tunneling would be to use TST with a semiclassical tunneling correction for temperatures above and around T_c and connect those to HQTST results in the deep tunneling regime below T_c. This however requires further investigation.

As a final point we note that the quantum instanton results shown in Figure 4 are larger than the quantum dynamics results by factors of about 2 to 3 over the temperature range shown. Since the same potential energy surface has been used, errors in the surface can be ignored in this comparison. In the quantum dynamics calculations, possible inaccuracies could arise from the use of the *J*-shifting approximation and the neglect of the vibrational angular momenta Hamiltonian. It has been possible to assess the accuracy of the *J*-shifting approximation for several
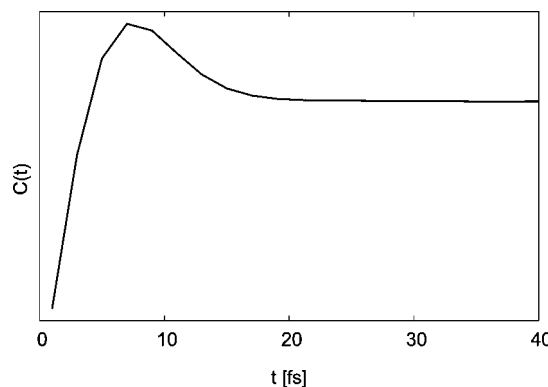
reactions, viz., Cl + H$_2$,[81−83] O + HCl,[84−87] H$_2$ + OH[85,88,89] and HCl + OH.[90] The *J*-shifting approximation generally works best when the moments of inertia change little, as a percentage of their values, over the geometry range which determines if reaction occurs, which typically is the case if the barrier is pronounced. This suggests that for H + CH$_4$ the *J*-shifting approximation for the rate constants should only cause errors below 10%. Similar arguments also indicate that the neglect of the vibrational angular momenta do also not cause relevant errors. The calculations themselves are converged to within 10% or better. Thus, the error of the quantum dynamics calculation of the rate constants should not exceed 20%.

Also the quantum instanton calculations are expected to work well for the H + CH$_4$ reaction. Issues to consider in the quantum instanton calculations are recrossing and convergence with respect to number of samples and other parameters. The quantum dynamics show that the flux−flux correlation function quickly settles on its long-term value and before that it only overshoots by less than 30%; see Figure 7. This overshoot is a combined effect of recrossing and tunneling. These effects are not separable, but the small overshoot indicates that recrossing is not a major effect. Overall the difference between the quantum dynamics and quantum instanton results is somewhat larger than what might have been expected, but we do not have an explicit explanation for this.

**4.3. Convergence Properties of HQTST Calculations.** Figures 8 and 9 illustrate how the HQTST rate constants converge when the number of images used is increased. The results are displayed as ratios of the instanton rate constant with *P* images over the one calculated using 1024 images. Since the results from using 768 and 1024 images differ by at most 20% (Figure 9) the 1024-image calculations are assumed to be converged to within at least 20% in the calculated rate constants. Therefore the 1024-image rate constants are taken as the converged reference limit. As discussed in section 3.2, the instanton calculations will start to deteriorate once a second imaginary frequency appears. For 16 images this happens already at 250 K, for 32 images below 200 K, and for 64 images below 100 K. For this reason no results are included for temperatures where a second imaginary frequency is present. In the figures *P* refers to the total number of images in the CFPs. As discussed in section 3.2 only half the images are actively taken into account in the optimization of the instanton.

From Figure 8 it can be seen that convergence with respect to the number of images is from below when the temperature is above 200 K and from above when the temperature is below 200 K. The 16-image rate constants are within 20% of the converged values, the 32-image rate constants are within 5%,
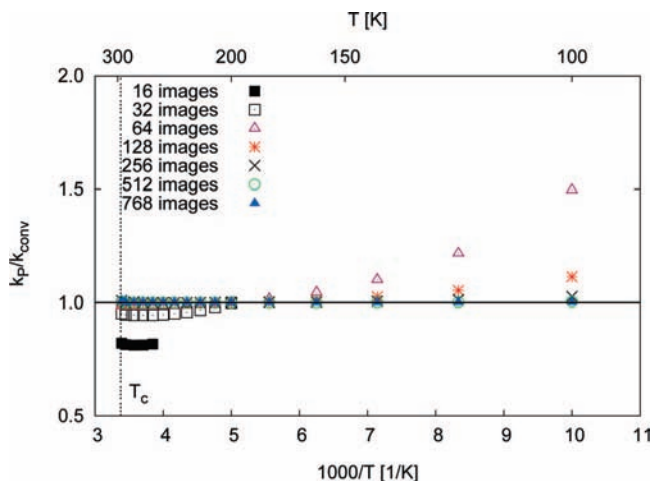
Figure 8. Convergence of the HQTST rate constants with number of images for $H + CH_4 \rightarrow CH_3 + H_2$ using PJEG. The ratio of rate constants for calculations with P images and the converged rate constants (1024-image calculations) is shown as a function of temperature.
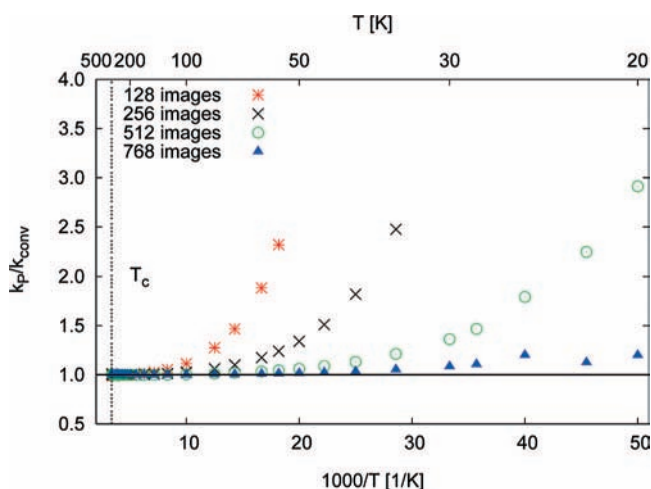

Figure 9. Convergence of the HQTST rate constants with a number of images for $H + CH_4 \rightarrow CH_3 + H_2$ using PJEG. Ratios are given as in Figure 8.

and above 200 K the 64-image rate constants are within 1% of the converged values. At their lowest reliable temperature, 100 K, the 64-image rate constants are 50% higher than the converged ones. At this temperature the 128-image rate constant is 11% off the converged value and the 256-image rate constant is only 3% off. At still lower temperatures (Figure 9) the rate constants for 128 and 256 images are less than a factor 3 higher than the converged result at their respective lowest reliable temperatures. At 35 K the 256-image rate constant is 2.5 times larger than the 1024-image rate constant, the 512-image rate constant 1.2 times larger, and the 768-image rate constant 1.05 times larger. To conclude, convergence is rapid with respect to the number of images and for all temperatures studied the calculated rate constants remain within the same order of magnitude as long as no second imaginary frequency appears.

4.4. Visualizing Quantum Tunneling with HQTST. Apart from the fact that HQTST calculations seem to be an efficient way to calculate quantum rate constants, they have an additional strength as providing visual diagnostic tools for studies of tunneling in molecular systems. The instantons can be visualized in a straightforward way and be compared to the classical saddle point. HQTST also accounts for quantum effects by lowering
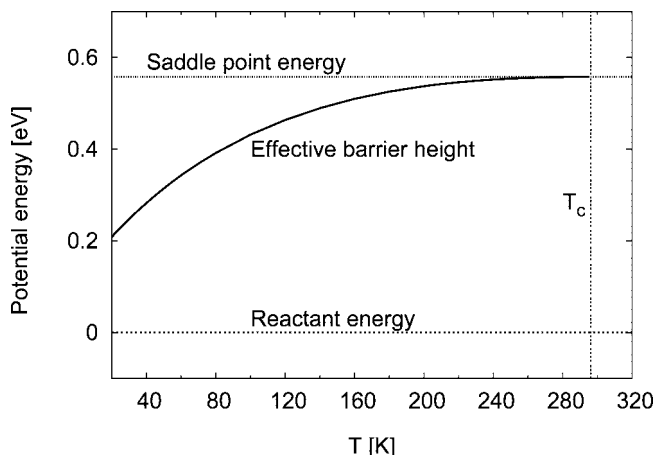

Figure 10. HQTST effective barrier height vs temperature, for $H + CH_4 \rightarrow CH_3 + H_2$ using PJEG.
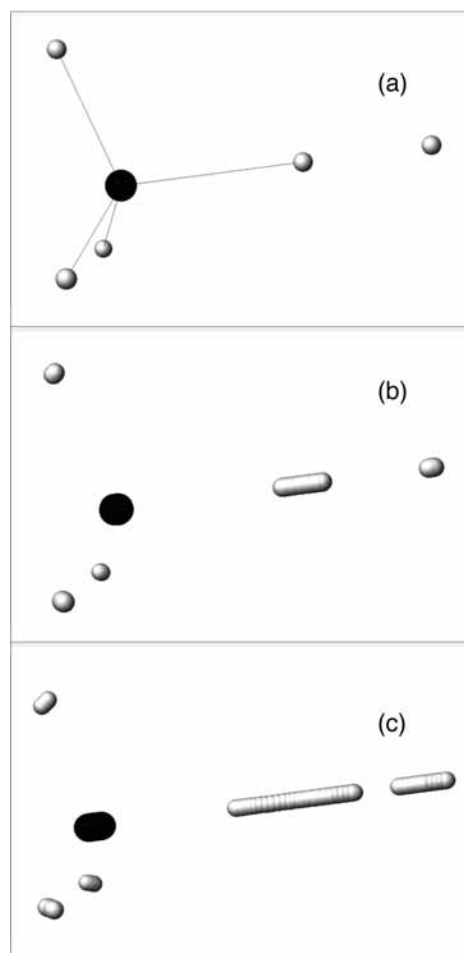
Figure 11. HQTST instantons at (a) the crossover temperature $T_c = 296$ K (coinciding with the classical saddle point), (b) $T = 200$ K, and (c) $T = 100$ K.

the effective barrier height, as defined by eq 7. This is illustrated in Figure 10 where the effective barrier height is shown as a function of temperature.

As the temperature is lowered the instanton becomes more delocalized. This is illustrated in Figure 11 where it is seen how the instanton, on PJEG, becomes more and more spread out as the temperature is lowered from the crossover temperature $T_c = 296$ K through 200 to 100 K. It is clear that it is the reactive atom that delocalizes the most. At 100 K it is apparent that

Comparison of H + CH$_4$ Reaction Rates

J. Phys. Chem. A, Vol. 113, No. 16, 2009 **4477**
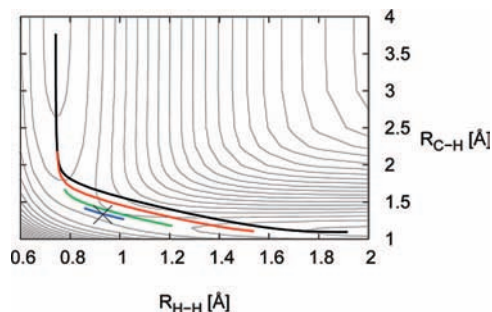
Figure 12. HQTST instantons at $T = 280$ K (blue), $T = 200$ K (green), $T = 100$ K (red), and $T = 20$ K (black). The potential is shown as a function of the two bonds directly involved in the reaction with other coordinates optimized to give the lowest potential energy. The contours have a spacing of 0.2 eV. The cross marks the position of the saddle point.

also the carbon atom plays an active role in the tunneling event as it is clearly quite delocalized. Figure 11 also shows the classical saddle point in (a) since the instanton collapses onto it at T_c.

It is well-known that as the temperature is lowered, the reaction "cuts the corner" more and more, i.e., deviates from the minimum energy path. The instantons in Figure 12 clearly illustrate this effect. Again the delocalization of the instanton is seen. As was discussed in section 4.2 in connection to CVT/ZCT and CVT/μOMT tunneling does not seem to lead to strong corner-cutting effects close to T_c. This is seen for the instanton at 280 K, which lies quite close to the saddle point and the MEP. At the lower temperatures the instantons move off the MEP to an increasingly larger extent. This illustrates why the CVT/ZCT rate constants, in which tunneling paths follow the MEP, fall increasingly below the HQTST and CVT/μOMT rate constants as temperature is decreased.

5. Conclusions

Thermal rate constants have been calculated for the H + CH$_4$ $\rightarrow$ CH$_3$ + H$_2$ reaction employing the potential energy surface of Espinosa-García.[16] Two theoretical approaches have been employed. First we employ the multiconfigurational time-dependent Hartree method combined with flux correlation functions. In this way rate constants in the range 225−400 K have been obtained. These were compared with previous results using the same theoretical method but the potential energy surface of Wu et al.[22] It was found that the Espinosa-García surface results in larger rate constants. This is connected to the procedure Espinosa-García used to obtain the surface, which is semiempirical.

Second, a harmonic quantum transition state theory (HQTST) implementation of instanton theory was used to obtain rate constants in a temperature interval from 20 K up to the crossover temperature at 296 K. In comparing to the accurate quantum dynamics results, we noticed that the HQTST rate constant is larger by a factor of about 3. Part of this may relate to the fact that HQTST treats the reactant(s) harmonically, while some of the anharmonicity at the transition state is accounted for.

We compared the quantum dynamics rate constants obtained in the present work to the previously obtained quantum instanton rate constants[64] on the same surface. The rates agree to within a factor of about 2 at 400 K and 3 at 300 K.

Finally, we used the instanton to illustrate delocalization and corner cutting in the H + CH$_4$ $\rightarrow$ CH$_3$ + H$_2$ reaction.

References and Notes

(1) Takayanagi, T. *J. Chem. Phys.* **1996**, *104*, 2237.
(2) Yu, H.-G.; Nyman, G. *J. Chem. Phys.* **1999**, *111*, 3508.
(3) Wang, M. L.; Li, Y.; Zhang, J. Z. H.; Zhang, D. H. *J. Chem. Phys.* **2000**, *113*, 1802.
(4) Wang, D.; Bowman, J. M. *J. Chem. Phys.* **2001**, *115*, 2055.
(5) Yu, H.-G. *Chem. Phys. Lett.* **2000**, *332*, 538.
(6) Palma, J.; Echave, J.; Clary, D. C. *J. Phys. Chem. A* **2002**, *106*, 8256.
(7) Wang, M. L.; Zhang, J. Z. H. *J. Chem. Phys.* **2002**, *117*, 3081.
(8) Wang, M. L.; Zhang, J. Z. H. *J. Chem. Phys.* **2002**, *116*, 6497.
(9) Yang, M.; Zhang, D. H.; Lee, S.-Y. *J. Chem. Phys.* **2002**, *117*, 9539.
(10) Wang, D. *J. Chem. Phys.* **2002**, *117*, 9806.
(11) Wang, D. *J. Chem. Phys.* **2003**, *118*, 1184.
(12) Pu, J.; Corchado, J. C.; Truhlar, D. G. *J. Chem. Phys.* **2001**, *115*, 6266.
(13) Pu, J.; Truhlar, D. G. *J. Chem. Phys.* **2002**, *117*, 1479.
(14) Pu, J.; Truhlar, D. G. *J. Chem. Phys.* **2001**, *114*, 1468.
(15) Pu, J.; Truhlar, D. G. *J. Chem. Phys.* **2002**, *117*, 10675.
(16) Espinosa-García, J. *J. Chem. Phys.* **2002**, *116*, 10664.
(17) Kerkeni, B.; Clary, D. C. *J. Chem. Phys.* **2004**, *120*, 2308.
(18) Zhao, Y.; Yamamoto, T.; Miller, W. H. *J. Chem. Phys.* **2004**, *120*, 3100.
(19) Huarte-Larrañaga, F.; Manthe, U. *J. Chem. Phys.* **2000**, *113*, 5115.
(20) Huarte-Larrañaga, F.; Manthe, U. *J. Phys. Chem. A* **2001**, *105*, 2522.
(21) Huarte-Larrañaga, F.; Manthe, U. *J. Chem. Phys.* **2002**, *116*, 2863.
(22) Wu, T.; Werner, H.-J.; Manthe, U. *Science* **2004**, *306*, 2227.
(23) Wu, T.; Werner, H.-J.; Manthe, U. *J. Chem. Phys.* **2006**, *124*, 164307.
(24) van Harrevelt, R.; Nyman, G.; Manthe, U. *J. Chem. Phys.* **2007**, *126*, 084303.
(25) Nyman, G.; van Harrevelt, R.; Manthe, U. *J. Phys. Chem. A* **2007**, *111*, 10331.
(26) Huarte-Larrañaga, F.; Manthe, U. *J. Chem. Phys.* **2002**, *117*, 4635.
(27) Meyer, H.-D.; Manthe, U.; Cederbaum, L. S. *Chem. Phys. Lett.* **1990**, *165*, 73.
(28) Manthe, U.; Meyer, H.-D.; Cederbaum, L. S. *J. Chem. Phys.* **1992**, *97*, 3199.
(29) Yamamoto, T. *J. Chem. Phys.* **1960**, *33*, 281.
(30) Miller, W. H. *J. Chem. Phys.* **1974**, *61*, 1823.
(31) Miller, W. H.; Schwartz, S. D.; Tromp, J. W. *J. Chem. Phys.* **1983**, *79*, 4889.
(32) (a) Arnaldsson, A.; Bligaard, T.; Jónsson, H. In preparation. (b) Arnaldsson, A. PhD thesis; University of Washington, 2007.
(33) Marcus, R. A. *J. Chem. Phys.* **1966**, *45*, 4493.
(34) Garrett, B. C.; Truhlar, D. G. *J. Am. Chem. Soc.* **1979**, *101*, 4534.
(35) Truhlar, D. G.; Isaacson, A. D.; Garrett, B. C. In *The Theory of Chemical Reactions*; Baer, M., Ed.; CRC: Boca Raton, FL, 1985; Vol. 4.
(36) Liu, Y.-P.; Lynch, G. C.; Truong, T. N.; Lu, D.-h.; Truhlar, D. G *J. Am. Chem. Soc.* **1993**, *115*, 2408.
(37) Liu, Y.-P.; Lu, D.-h.; González, A.; Truhlar, D. G.; Garrett, B. C *J. Am. Chem. Soc.* **1993**, *115*, 7806.
(38) Fernández-Ramos, A.; Truhlar, D. G. *J. Chem. Phys.* **2001**, *114*, 1491.
(39) Fernandez-Ramos, A.; Ellingson, B. A.; Garrett, B. C.; Truhlar, D. G. In *Reviews in Computational Chemistry*; Lipkowitz, K. B., Cundari, T. R., Eds.; Wiley-VCH: Hoboken, NJ, 2007; Vol. 23, p 125.
(40) Corchado, J. C.; et al. *POLYRATE−Version 9.6*; University of Minnesota: Minneapolis, MN, 2007.
(41) Feynman, R. P.; Hibbs, A. R. *Quantum Mechanics and Path Integrals*; McGraw-Hill: New York, 1965.
(42) Feynman, R. P. *Statistical Mechanics*; Addison-Wesley: Reading, MA, 1998.
(43) Gillan, M. *J. Phys. C: Solid State Phys.* **1987**, *20*, 3621.
(44) Voth, G. A.; Chandler, D.; Miller, W. H. *J. Chem. Phys.* **1989**, *91*, 7749.
(45) Messina, M.; Schenter, G. K.; Garrett, B. C. *J. Chem. Phys.* **1995**, *103*, 3430.
(46) Mills, G.; Schenter, G. K.; Makarov, D. E.; Jónsson, H. *Chem. Phys. Lett.* **1997**, *278*, 91.
(47) Pollak, E.; Liao, J.-L. *J. Chem. Phys.* **1998**, *108*, 2733.
(48) Jang, S.; Voth, G. A. *J. Chem. Phys.* **2000**, *112*, 8747.
(49) Miller, W. H.; Zhao, Y.; Ceotto, M.; Yang, S. *J. Chem. Phys.* **2003**, *119*, 1329.

4478 *J. Phys. Chem. A, Vol. 113, No. 16, 2009*

Andersson et al.

(50) Miller, W. H. *J. Chem. Phys.* **1975**, *62*, 1899.

(51) Coleman, S. *Phys. Rev. D* **1977**, *15*, 2929.

(52) Callan, C. G., Jr.; Coleman, S. *Phys. Rev. D* **1977**, *16*, 1762.

(53) Coleman, S. In *The Whys of Subnuclear Physics*; Zichichi, A., Ed.; Plenum: New York, 1979.

(54) Schäfer, T.; Shuryak, E. V. *Rev. Mod. Phys.* **1998**, *70*, 323.

(55) Langer, J. S. *Ann. Phys.* **1967**, *41*, 108.

(56) Langer, J. S. *Ann. Phys.* **1969**, *54*, 258.

(57) Affleck, I. *Phys. Rev. Lett.* **1981**, *46*, 388.

(58) Chapman, S.; Garrett, B. C.; Miller, W. H. *J. Chem. Phys.* **1975**, *63*, 2710.

(59) Benderskii, V. A.; Makarov, D. E.; Wight, C. A. *Adv. Chem. Phys.* **1994**, *88*, 1.

(60) Siebrand, W.; Smedarchina, Z.; Zgierski, M. Z.; Fernández-Ramos, A. *Int. Rev. Phys. Chem.* **1999**, *18*, 5.

(61) Smedarchina, Z.; Fernández-Ramos, A.; Siebrand, W. *J. Comput. Chem.* **2001**, *22*, 787.

(62) Hänggi, P.; Talkner, P.; Borkovec, M. *Rev. Mod. Phys.* **1990**, *62*, 251.

(63) Jordan, M. J. T.; Gilbert, R. G. *J. Chem. Phys.* **1995**, *102*, 5669.

(64) Zhao, Y.; Yamamoto, T.; Miller, W. H. *J. Chem. Phys.* **2004**, *120*, 3100.

(65) Matzkies, F.; Manthe, U. *J. Chem. Phys.* **1998**, *108*, 4828.

(66) Manthe, U.; Miller, W. H. *J. Chem. Phys.* **1993**, *99*, 3411.

(67) Matzkies, F.; Manthe, U. *J. Chem. Phys.* **1997**, *106*, 2646.

(68) Bowman, J. M. *J. Phys. Chem.* **1991**, *95*, 4960.

(69) Manthe, U.; Huarte-Larrañaga, F. *Chem. Phys. Lett.* **2001**, *349*, 321.

(70) Bowman, J. M.; Wang, D.; Huang, X.; Huarte-Larrañaga, F.; Manthe, U. *J. Chem. Phys.* **2001**, *114*, 9683.

(71) Manthe, U.; Matzkies, F. *Chem. Phys. Lett.* **1998**, *282*, 442.

(72) Makarov, D. E.; Topaler, M. *Phys. Rev. E* **1995**, *52*, 178.

(73) Chandler, D.; Wolynes, P. G. *J. Chem. Phys.* **1981**, *74*, 4078.

(74) Manthe, U. *J. Chem. Phys.* **1995**, *102*, 9205.

(75) Manthe, U. *J. Theor. Comput. Chem.* **2002**, *1*, 153.

(76) Henkelman, G.; Jónsson, H. *J. Chem. Phys.* **1999**, *111*, 7010.

(77) Olsen, R. A.; Kroes, G. J.; Henkelman, G.; Arnaldsson, A.; Jónsson, H. *J. Chem. Phys.* **2004**, *121*, 9776.

(78) Wigner, E. *Z. Phys. Chem. B* **1932**, *19*, 203.

(79) Wigner, E. *Trans. Faraday Soc.* **1938**, *34*, 29.

(80) Skodje, R. T.; Truhlar, D. G. *J. Phys. Chem.* **1981**, *85*, 624.

(81) Mielke, S. L.; Allison, T. C.; Truhlar, D. G.; Schwenke, D. W. *J. Phys. Chem.* **1996**, *100*, 13588.

(82) Wang, H.; Thompson, W. H.; Miller, W. H. *J. Chem. Phys.* **1997**, *107*, 7194.

(83) Manthe, U.; Bian, W.; Werner, H.-J. *Chem. Phys. Lett.* **1999**, *313*, 647.

(84) Nobusada, K.; Nakamura, H. *J. Phys. Chem. A* **1999**, *103*, 6715.

(85) Bowman, J. M. *Theor. Chem. Acc.* **1998**, *108*, 125.

(86) Thompson, W. H.; Miller, W. H. *J. Chem. Phys.* **1997**, *106*, 142.

(87) Matzkies, F.; Manthe, U. *J. Chem. Phys.* **2000**, *112*, 130.

(88) Zhang, D. H.; Lee, S.-Y. *J. Chem. Phys.* **1999**, *110*, 4435.

(89) Manthe, U.; Matzkies, F. *J. Chem. Phys.* **2000**, *113*, 5725.

(90) Huarte-Larrañaga, F.; Manthe, U. *J. Chem. Phys.* **2003**, *118*, 8261.